Faraday Discussions

Accepted Manuscript

This manuscript will be presented and discussed at a forthcoming Faraday Discussion meeting. All delegates can contribute to the discussion which will be included in the final volume.

Register now to attend! Full details of all upcoming meetings: http://rsc.li/fd-upcoming-meetings

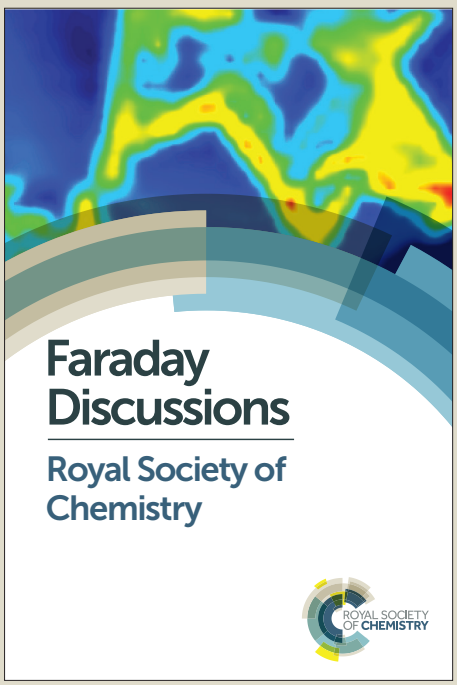

This is an *Accepted Manuscript*, which has been through the Royal Society of Chemistry peer review process and has been accepted for publication.

Accepted Manuscripts are published online shortly after acceptance, before technical editing, formatting and proof reading. Using this free service, authors can make their results available to the community, in citable form, before we publish the edited article. We will replace this *Accepted Manuscript* with the edited and formatted *Advance Article* as soon as it is available.

You can find more information about *Accepted Manuscripts* in the Information for Authors.

Please note that technical editing may introduce minor changes to the text and/or graphics, which may alter content. The journal's standard Terms & Conditions and the Ethical guidelines still apply. In no event shall the Royal Society of Chemistry be held responsible for any errors or omissions in this *Accepted Manuscript* or any consequences arising from the use of any information it contains.

ROYAL SOCIETY OF CHEMISTRY

www.rsc.org/faraday_d

CREATED USING THE RSC LaTeX PCCP ARTICLE TEMPLATE – SEE www.rsc.org/electronicfiles FOR DETAILS
PAPER www. rsc.org/faraday_d | Faraday Discussions

Dirac dispersion in photonic hypercrystals

Evgenii E. Narimanov[a]

Received Xth XXXXXXXXXX 20XX, Accepted Xth XXXXXXXXX 20XX
First published on the web Xth XXXXXXXXXX 200X
DOI: 10.1039/c000000x

Photonic hypercrystals – the recently introduced concept of artificial optical media that combines the properties of hyperbolic metamaterials and photonic crystals [*E. Narimanov, Phys. Rev. X* 4, 041014 (2014)] – can support Dirac cone dispersion at a finite frequency.

1 Introduction

The cornucopia of new physical phenomena in graphene[1,2] arising from Dirac cone dispersion of its free carriers, lead to the search for similar behavior in optical systems.[3–6] Dirac cones were found in coupled waveguide arrays[7] as well as in photonic crystals[3–6,8,9] and metamaterials,[8] thus opening the way to the study of such non-trivial phenomena as Klein tunneling paradox[10] and Shrödinger's "zitterbewegung"[11] that were so far believed to lie entirely within the realm of quantum physics and quantum electrodynamics, and even to possible practical applications of this behavior in actual photonic devices. However, optical systems that are currently known to support Dirac cone dispersion, generally rely on spatial variations in at least two or even in all three dimensions – which severely limits their applicability to practical applications.

In the present paper, we demonstrate that planar optical composites can also support propagating waves with Dirac dispersion. This behavior however cannot be found in the "regular" planar optical media, but relies on the new physics introduced by the recently discovered photonic hypercrystals.[12] These novel composite media are essentially hyperbolic metamaterials[13] with a periodic variation of electromagnetic response properties on a subwavelength scale, and combine the properties of metamaterials and photonic crystals. The resulting effect on the wave propagation and dispersion by bandgap formation in what is essentially the metamaterial limit, offers an unprecedented degree of control of light propagation in photonic hypercrystals – and allows for the formation of Dirac dispersion cones in the hypercrystal phase space.

As photonic hypercrystals can be assembled entirely within the restrictions of planar fabrication technology, this offers a unique opportunity to bring the exciting physics offered by Dirac cone dispersion, such as e.g. Klein tunneling or Shrödinger's zitterbewegung, to the realm of practical applications in nanophotonics.

[a] *School of Electrical and Computer Engineering and Birck Nanotechnology Center, Purdue University, West Lafayette, IN 47907, USA*

2 Photonic Hypercrystals: the concept

Metamaterials[14] and photonic crystals[15] currently represent two primary building blocks for advanced nanophotonic devices. With the goal of ultimate control over the light propagation, an artificial optical material must rely on either the effect of a subwavelength pattern that changes the average electromagnetic response of the medium, or on Bragg scattering of light due to a periodic variation that is comparable to the wavelength. Because of this inherent scale separation, the corresponding metamaterial and photonic crystal concepts are generally considered mutually exclusive within the same environment.

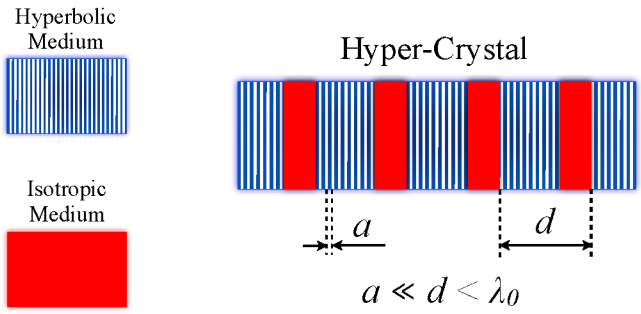

Fig. 1 A planar hypercrystal is formed by introducing a periodic variation in a hyperbolic medium, with the period smaller than the free-space wavelength $d < \lambda_0$, but well above the unit cell size of the hyperbolic (meta)material: $d \gg a$. The desired periodic variation can be achieved by introducing a second medium (which could be either a metal, or a dielectric, or another hyperbolic medium with a different dielectric permittivity tensor) in the design of the composite.

The situation is however dramatically different in the world of hyperbolic metamaterials,[13] where the opposite signs of the dielectric permittivity components in two orthogonal directions ($\mathrm{Re}[\varepsilon_n]\,\mathrm{Re}[\varepsilon_\tau] < 0$) lead to a hyperbolic dispersion of TM-polarized propagating waves

$$\frac{k_n^2}{\varepsilon_\tau} + \frac{k_\tau^2}{\varepsilon_n} = \frac{\omega^2}{c^2} \qquad (1)$$

with the wave numbers unlimited by the frequency ω. As a result, a periodic variation in the dielectric permittivity, regardless of how small is its period d (see Fig. 1), will necessarily cause Bragg scattering of these high-k waves, leading to the formation of photonic bandgaps in both the wavenumber and the frequency domains. This behavior is illustrated in Fig. 2, where we show the dispersion diagram for an example of such photonic hypercrystal. Note that in the entire frequency range shown in this figure, the spatial period of the hypercrystal is below one tenth of the corresponding free-space wavelength.

As long as the hyperbolic dispersion of Eqn. (1) remains adequate for the description of the hyperbolic metamaterial component of the hypercrystal, the

pattern of allowed and forbidden bands seen in Fig. 2, proliferates to ever higher wavenumbers. However, eventually the local wavelength $\lambda \equiv 2\pi/k$ becomes comparable to the unit cell size a of the hyperbolic medium (see Fig. 1), effectively terminating this behavior. The hypercrystal regime is therefore limited to $k \leq 1/a$ and can only be observed in the composites with

$$a \ll d < \lambda_0, \tag{2}$$

where λ_0 is the free-space wavelength. The resulting restrictions however can be substantially relaxed with the use of natural hyperbolic media such as e.g. sapphire[16], graphite[17], TGS[18–20] or bismuth[21–24], when Eqn. (2) reduces to simply $d < \lambda_0$.

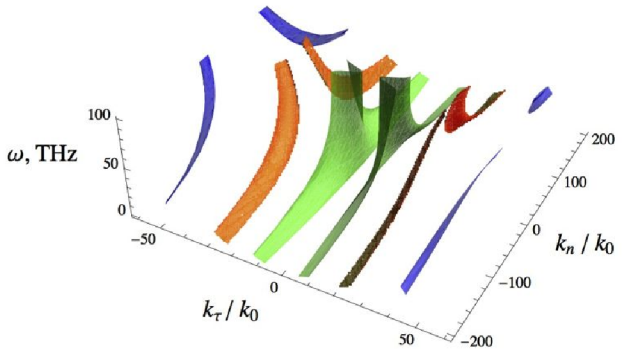

Fig. 2 The dispersion diagram of a photonic hypercrystal. The hypercrystal unit cell is formed by 250 nm of $In_{0.53}Ga_{0.47}As$: $Al_{0.48}In_{0.52}As$ semiconductor hyperbolic metamaterial[25] with 5 μm plasma wavelength, followed by 250 nm dielectric layer of $Al_{0.48}In_{0.52}As$. k_n and k_τ represent the wavevector components that are respectively normal and tangential to the layers form in the hypercrystal, $k_0 \equiv \omega/c$ is the free-space wavenumber.

3 Dirac Points in Hypercrystals

In its simplest realization, when a planar hypercrystal is formed by interleaving layers of hyperbolic and isotropic media (which can be either dielectric ($\mathrm{Re}[\varepsilon] > 0$) or metallic ($\mathrm{Re}[\varepsilon] < 0$)), the inversion symmetry of the composite allows to classify the TM-propagating modes ($\mathbf{B} = B\,\hat{\mathbf{n}}$ and $\mathbf{E} \perp \hat{\mathbf{n}}$, where $\hat{\mathbf{n}}$ is the unit vector normal to the layers - see Fig. 1) in terms of the parity "quantum number" $p = \pm 1$, with the standard Bloch states expressed as linear combinations of the even and odd modes $\mathbf{B}_{p=1}(\omega, \mathbf{r}) \pm i\,\mathbf{B}_{p=-1}(\omega, \mathbf{r})$. It is the accidental degeneracy between the states of different parity that is the key to the formation of Dirac cones in photonic hypercrystals.

For the TM-polarized modes propagating parallel to the layers forming the hypercrystal, and thus corresponding to the Bloch momentum $k_n = 0$, we obtain

$$\sin\left(\frac{k_h d_h}{2}\right)\cos\left(\frac{k_i d_i}{2}\right) + \left(\frac{\varepsilon_\tau}{\varepsilon_i}\frac{k_i}{k_h}\right)^p \cos\left(\frac{k_h d_h}{2}\right)\sin\left(\frac{k_i d_i}{2}\right) = 0 \tag{3}$$

where ε_i is the dielectric permittivity of the isotropic medium (see Fig. 1),

$$\varepsilon_h = \begin{pmatrix} \varepsilon_\tau & 0 & 0 \\ 0 & \varepsilon_\tau & 0 \\ 0 & 0 & \varepsilon_n \end{pmatrix} \quad (4)$$

is the dielectric permittivity tensor of the hyperbolic medium, k_h the wavenumber in the hyperbolic layers

$$k_h = \sqrt{\varepsilon_\tau \left(\frac{\omega^2}{c^2} - \frac{k_\tau^2}{\varepsilon_n} \right)}, \quad (5)$$

and k_i is the wavenumber in the layers formed by the isotropic medium

$$k_i = \sqrt{\varepsilon_i \frac{\omega^2}{c^2} - k_\tau^2}. \quad (6)$$

Here k_τ is the tangential component of the wavevector ($B \sim \exp(ik_\tau x)$), while d_h and d_i are the thicknesses of the hyperbolic and isotropic layers.

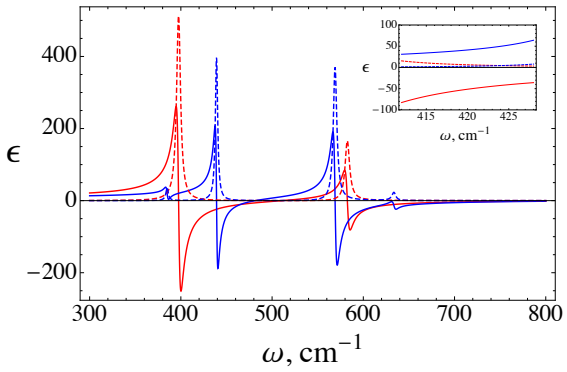

Fig. 3 The dielectric permittivity tensor of sapphire monocrystal in the Restrahlen band.[16] Red and blue lines correspond respectively to the permittivities parallel and perpendicular to the *C*-axis of the sapphire crystal. Real and imaginary parts of the permittivity are represented by solid and dotted lines. The inset shows the range near the free-space wavelength of 24 μm (≈ 417 cm^{-1}) that supports one of the low-loss hyperbolic bands in sapphire.

As follows from Eqn. (3), the "even" (parity $p = 1$) and "odd" ($p = -1$) "guided" modes propagating parallel to the layers of the hypercrystal, are degenerate when

$$\frac{\varepsilon_\tau}{\varepsilon_i} \frac{k_i}{k_h} = 1, \quad (7)$$

corresponding to the in-plane momentum

$$k_\tau = k_B \equiv \frac{\omega}{c} \sqrt{\varepsilon_i \frac{1 - \varepsilon_i/\varepsilon_\tau}{1 - \varepsilon_i^2/(\varepsilon_n \varepsilon_\tau)}} \quad (8)$$

which for a lossless system corresponds to the Brewser's angle at the interface of the isotropic dielectric ($\varepsilon_i > 0$) and the hyperbolic medium[25]. The frequency corresponding to this accidental degeneracy point, is then given by

$$\omega_0 = \frac{2\pi c\, m}{\varepsilon_\tau d_h + \varepsilon_i d_i}\sqrt{\varepsilon_\tau \frac{1-\varepsilon_i^2/(\varepsilon_n\varepsilon_\tau)}{1-\varepsilon_i/\varepsilon_n}}, \tag{9}$$

where m is a (positive) integer. Note that strong dispersion of the dielectric permittivity common in hyperbolic media, makes Eqn. (9) a nontrivial equation for ω_0. Furthermore, losses inevitable in the hyperbolic media, lead to a nonzero imaginary part of ω_0.

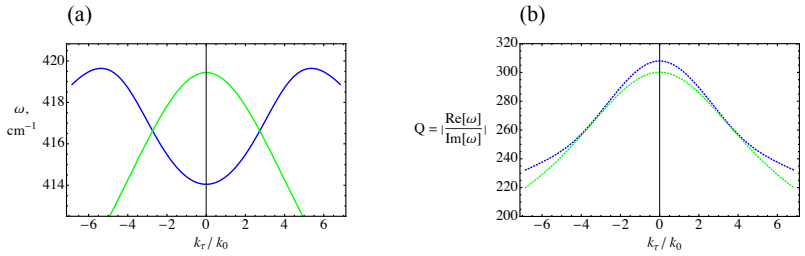

Fig. 4 The frequency ω (panel (a)) and the "Q-factor" (panel (b)) vs. in-plane wavenumber k_τ for $m = 1$ even (green line) and odd (blue line) modes propagating parallel to the layers of silicon-sapphire hypercrystal, for $d_h = 3.55$ μm and $d_i = 0.676$ μm.

We will illustrate this behavior using the example of a hypercrystal formed by alternating layers of silicon and sapphire – two complimentary materials which form the backbone of the silicon-on-sapphire hetero-epitaxial process[26]. In mid-IR range, sapphire offers several low-loss hyperbolic bands (see Fig. 3), while silicon behaves as a transparent dielectric with the permittivity of $\varepsilon_{\rm Si} \approx 11.7$. In Fig. 4 we plot the dispersion $\omega(k_\tau)$ of the guided modes for the silicon-sapphire hypercrystal, with the unit cell formed by 676 nm of silicon and 3.55 μm of sapphire.

Expanding Eqn. (3) near the degeneracy point (k_B, ω_0), we obtain

$$A_0\frac{\omega-\omega_0}{\omega_0} = (B_0 + p\,C_0)\frac{k_\tau - k_B}{k_B} + O\left[\left(\frac{\omega-\omega_0}{\omega_0}\right)^2, \left(\frac{k_\tau-k_B}{k_B}\right)^2\right] \tag{10}$$

where $p = \pm 1$ is the mode parity, and

$$\begin{aligned} A_0 &= 1 + \frac{\pi mc}{\omega_0}\frac{\varepsilon_\tau d_h}{(\varepsilon_\tau d_h + \varepsilon_i d_i)^2}\sqrt{\varepsilon_\tau\frac{1-\varepsilon_i^2/\varepsilon_n\varepsilon_\tau}{1-\varepsilon_i/\varepsilon_n}} \\ &\times \left(\frac{\varepsilon_i}{\varepsilon_\tau}\frac{d\,(\varepsilon_\tau/\varepsilon_i)}{d\omega} + \frac{\varepsilon_i^2}{\varepsilon_n\varepsilon_\tau}\frac{\varepsilon_\tau-\varepsilon_i}{\varepsilon_n-\varepsilon_i}\frac{d\,(\varepsilon_n/\varepsilon_i)}{d\omega}\right), \end{aligned} \tag{11}$$

$$B_0 = \frac{2\pi mc}{\omega_0}\frac{\varepsilon_i d_h + \varepsilon_n d_i}{(\varepsilon_\tau d_h + \varepsilon_i d_i)^2}\frac{\varepsilon_\tau^{3/2}}{\varepsilon_n\sqrt{\varepsilon_i}}\frac{1-\varepsilon_i^2/\varepsilon_n\varepsilon_\tau}{(1-\varepsilon_i/\varepsilon_n)^{3/2}}\sqrt{1-\varepsilon_i/\varepsilon_\tau} \tag{12}$$

$$C_0 = \frac{2c}{\omega_0}\frac{1}{\varepsilon_\tau d_h + \varepsilon_i d_i}\left(\frac{\varepsilon_\tau}{\varepsilon_i}\right)^{3/2}\frac{\left(1-\varepsilon_i^2/\varepsilon_n\varepsilon_\tau\right)^2}{\left(1-\varepsilon_i/\varepsilon_n\right)^{3/2}}\sqrt{1-\varepsilon_i/\varepsilon_\tau} \times \sin\left(\frac{\pi m}{1+\frac{\varepsilon_\tau}{\varepsilon_i}\frac{d_h}{d_i}}\right)\cos\left(\frac{\pi m}{1+\frac{\varepsilon_i}{\varepsilon_\tau}\frac{d_i}{d_h}}\right) \quad (13)$$

For a dielectric photonic crystal, we find that $B_0 \pm C_0 > 0$, and the accidental degeneracy point at (k_B, ω_0) corresponds to the standard Brewser angle collapse of the photonic crystal bandgap.[15,27] In a hypercrystal however one finds the possibility of $(B_0+C_0)(B_0-C_0) < 0$, with the opposite signs of the group velocities of the even and odd guided modes. Furthermore, for $\mathrm{Re}[\varepsilon_n] < 0$ the magnitude of B_0 can be dramatically reduced – all the way to zero in the lossless limit, at

$$\frac{\varepsilon_n(\omega_0)}{\varepsilon_i(\omega_0)} = -\frac{d_h}{d_i}, \quad (14)$$

in which case Eqn. (10) can be expressed as

$$A_0\frac{\omega-\omega_0}{\omega_0} = \pm C_0\frac{k_\tau - k_B}{k_B} + O\left[\left(\frac{\omega-\omega_0}{\omega_0}\right)^2, \left(\frac{k_\tau-k_B}{k_B}\right)^2\right] \quad (15)$$

For a lossy system, Eqns. (9) and (14) cannot be simultaneously satisfied even for a complex ω_0. However, for the modes with $\mathrm{Re}[\omega] \gg \mathrm{Im}[\omega]$ (or equivalently $Q \equiv \mathrm{Re}[\omega]/\mathrm{Im}[\omega] \gg 1$), as in the case of the silicon-sapphire hypercrystal (see Fig. 4(b)), we can choose

$$\frac{d_i}{d_h} = -\mathrm{Re}\left[\frac{\varepsilon_n(\omega_0)}{\varepsilon_i(\omega_0)}\right], \quad (16)$$

which yields

$$A_0\frac{\omega-\omega_0}{\omega_0} = \pm C_0\frac{k_\tau-k_B}{k_B} + O\left[\left(\frac{\omega-\omega_0}{\omega_0}\right)^2, \left(\frac{k_\tau-k_B}{k_B}\right)^2, \frac{k_\tau-k_B}{k_B}\frac{\mathrm{Im}[\varepsilon]}{\mathrm{Re}[\varepsilon]}\right] \quad (17)$$

Eqns. (9) and (16) define the geometry of the hypercrystal unit cell and the "operational frequency" for the Dirac dispersion point.

For the calculation of the propagating waves in a planar hypercrystal for $k_n \neq 0$, we use the standard T-matrix approach[27] that can be generalized to the case of anisotropic material components.[12] This yields the unit cell transfer matrix

$$T \equiv \begin{pmatrix} T_{11} & T_{12} \\ T_{21} & T_{22} \end{pmatrix} \quad (18)$$

where

$$T_{11} = \left[\cos(k_h d_h) + \frac{i}{2}\left(\frac{k_h}{k_i}\frac{\varepsilon_i}{\varepsilon_\tau} + \frac{k_i}{k_h}\frac{\varepsilon_\tau}{\varepsilon_i}\right)\sin(k_h d_h)\right]\exp(ik_i d_i) \quad (19)$$

$$T_{12} = \frac{i}{2}\left(\frac{k_h}{k_i}\frac{\varepsilon_i}{\varepsilon_\tau} - \frac{k_i}{k_h}\frac{\varepsilon_\tau}{\varepsilon_i}\right)\sin(k_h d_h)\exp(-ik_i d_i) \quad (20)$$

$$T_{21} = -\frac{i}{2}\left(\frac{k_h}{k_i}\frac{\varepsilon_i}{\varepsilon_\tau} - \frac{k_i}{k_h}\frac{\varepsilon_\tau}{\varepsilon_i}\right)\sin(k_h d_h)\exp(ik_i d_i) \quad (21)$$

$$T_{22} = \left[\cos(k_h d_h) - \frac{i}{2}\left(\frac{k_h}{k_i}\frac{\varepsilon_i}{\varepsilon_\tau} + \frac{k_i}{k_h}\frac{\varepsilon_\tau}{\varepsilon_i}\right)\sin(k_h d_h)\right]\exp(-ik_i d_i) \quad (22)$$

In this approach, the magnetic field in the dielectric layer of the unit cell n (so that $(d_i+d_h)(n-1) < z < (d_i+d_h)(n-1)+d_i$), is given by

$$\begin{aligned}\mathbf{B}(\omega,x,z;k_\tau,k_n) &= \hat{\mathbf{y}}\,\exp(ik_\tau x + ik_n z)\\ &\times \{\alpha\exp[k_n(z-(d_i+d_h)(n-1))]\\ &+ \beta\exp[k_n(z-(d_i+d_h)(n-1))]\}\end{aligned} \quad (23)$$

where $\{\alpha,\beta\}$ is the eigenvector of the transfer matrix

$$T\begin{pmatrix}\alpha\\ \beta\end{pmatrix} = \exp[ik_n(d_h+d_i)]\begin{pmatrix}\alpha\\ \beta\end{pmatrix} \quad (24)$$

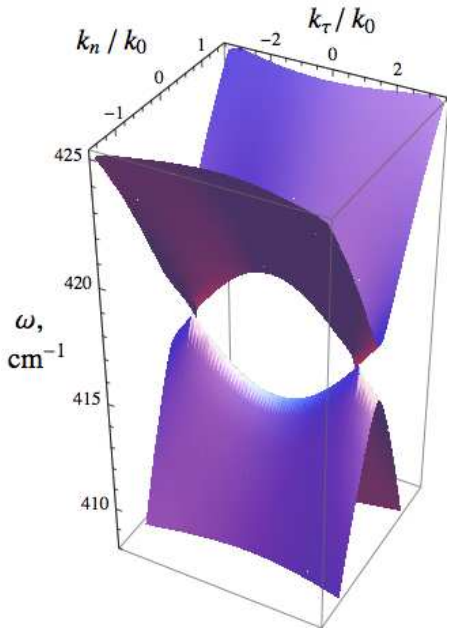

Fig. 5 The dispersion diagram for the silicon-sapphire hypercrystal, introduced in Fig. 4. The thickness of sapphire layers d_h is 3.55 μm and the width of the silicon layers d_i is 0.676 μm.

The dispersion of the propagating waves can then be obtained from the equation

$$\mathrm{Tr}[T] = 2\cos[ik_n(d_h+d_i)] \quad (25)$$

In Fig. 5 we show the dispersion diagram for the example of the silicon-sapphire hypercrystal that we introduced earlier. Note two Dirac cones in the phase space of the system at $(k_\tau, k_n) = (\pm k_B, 0)$, as predicted by our earlier analysis.

The new physics introduced by the presence of the Dirac dispersion cones in the phase space of the system, can only be explored if the corresponding states represent an example of "good" quasi-particles, with the lifetimes substantially exceeding the period of a single oscillation, $Q \equiv \omega\tau \gg 1$. With the mode lifetime defined by

$$\tau = \frac{1}{|\mathrm{Im}[\omega]|}, \tag{26}$$

for the mode Q-factor we obtain

$$Q = \left|\frac{\mathrm{Re}[\omega]}{\mathrm{Im}[\omega]}\right|. \tag{27}$$

In Fig. 6 we plot the Q-factor of the propagating modes for the frequency range in the proximity of the Dirac point. With Q-factors on the order of several hundred, the corresponding states should be easily accessible in experiment.

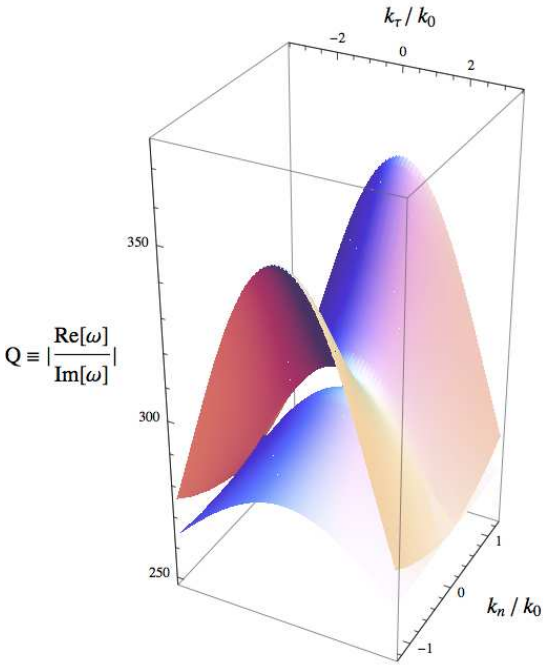

Fig. 6 The mode Q-factors for the silicon-sapphire hypercrystal in Figs. 4 and 5.

In addition to the Dirac points at $k_n = 0$ (see Fig. 5), planar hypercrystals also have similar singularities at the edge of the Brillouin zone ($k_n = \pm\frac{\pi}{d_h+d_i}$). These can be analyzed in a similar manner, starting from the "guided modes" that satisfy the boundary condition $B(z+d_h+d_i) = \pm\, i\, B(z)$, and one finds the behavior similar to the that of Dirac states near $k_n = 0$.

4 The Effective Hamiltonian near the Dirac point of a hypercrystal

Focusing on the Dirac point at $(k_\tau, k_n, \omega) = (k_B, 0, \omega_0)$, we expand Eqn. (25) in k_n, $k_\tau - k_B$ and $\omega - \omega_0$. The resulting straightforward calculation leads to the effective Hamiltonian

$$\mathcal{H}_{\text{eff}} = \begin{pmatrix} 0 & v_\tau (k_\tau - k_B) - i v_n k_n \\ v_\tau (k_\tau - k_B) + i v_n k_n & 0 \end{pmatrix} \tag{28}$$

such that

$$\mathcal{H}_{\text{eff}} \begin{pmatrix} \psi_1 \\ \psi_2 \end{pmatrix} = (\omega - \omega_0) \begin{pmatrix} \psi_1 \\ \psi_2 \end{pmatrix} \tag{29}$$

In terms of the Pauli matrices σ_x and σ_y, the effective Hamiltonian (28) can be expressed as

$$\mathcal{H}_{\text{eff}} = \sigma_x v_\tau (k_\tau - k_B) + \sigma_y v_n k_n \tag{30}$$

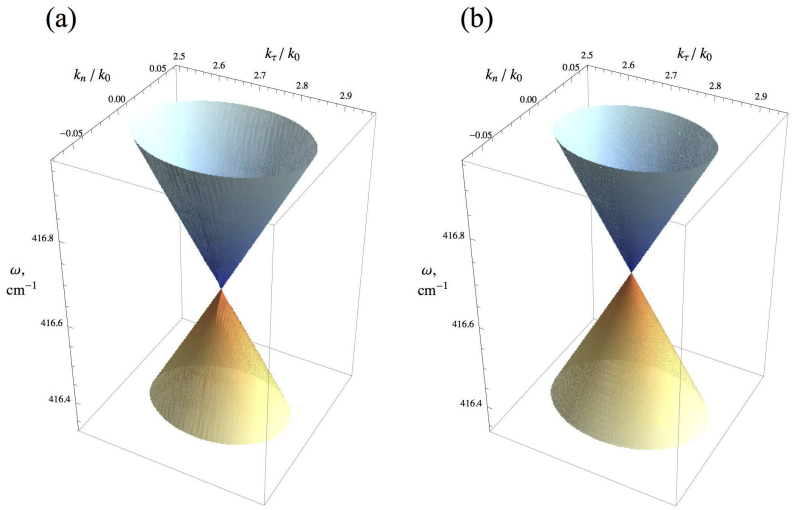

Fig. 7 The comparison of the exact dispersion diagram near the Dirac dispersion point of a silicon-sapphire hypercrystal (a) with the effective Hamiltonian approximation (b). Note small shift along the frequency axis that results from the losses in the material that are not fully accounted for in the analytical approximation of Eqns. (28) - (32).

Here,

$$v_\tau = c \,\text{Re}\left[\frac{C_0}{A_0}\right], \tag{31}$$

$$v_n = \text{Re}\left[\frac{\omega_0 (d_h + d_i)}{2\pi m A_0}\right], \tag{32}$$

where A_0 and C_0 are respectively defined by Eqns. (11) and (13).

In Fig. 7 we present the comparison of the exact dispersion diagram of the silicon-sapphire hypercrystal introduced earlier, to the effective Hamiltonian approximation of Eqns. (28) - (32). Note that, aside from the small frequency offset resulting from neglecting second-order cross-terms related to the loss in the hyperbolic media ($\sim O\left(\left(k_\tau - k_B\right) \mathrm{Im}\left[\varepsilon\right] / \mathrm{Re}\left[\varepsilon\right]\right)$ – see Eqn. (17)), one finds excellent agreement between the anisotropic Dirac-Weyl Hamiltonian (28) and the exact solution.

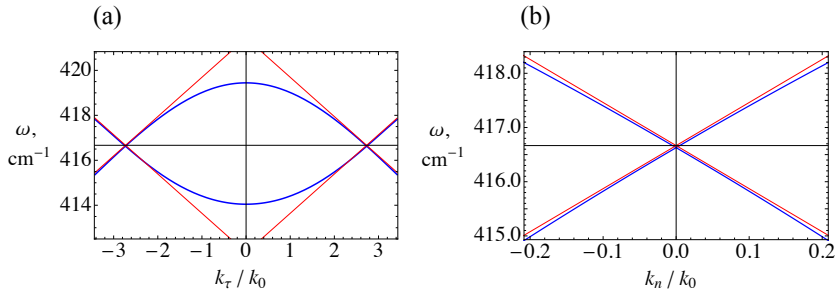

Fig. 8 The cross-sections of the silicon-sapphire hypercrystal dispersion diagram (Figs. 5, 7), through the Dirac points $k_\tau = \pm k_B$, $k_n = 0$, $\omega = \omega_0$, in k_τ (panel (a)) and k_n (panel (b)) directions. The blue curves correspond to the exact solution, while the red lines represent the effective Hamilatonian approximaion.

In Fig. 8 we present an alternative representation of this comparison, with the "cross-sections" of the phase space through the Dirac point in k_τ (Fig. 8(a)) and k_n (Fig. 8(b)) directions. Note that Fig. 8 shows a much broader frequency range than Fig. 7.

As the Dirac-Weyl Hamiltonian (28) proves an excellent approximation for the dynamics of the propagating waves in the hypercrystals near the accident degeneracy points, optical experiments in these composites can be used to study the optical equivalents of the many quantum-mechanical phenomena – from the zitterbewegung [11] to Klein tunneling [10]. Furthermore, the corresponding modulation of the transmission and reflection properties of the hypercrystal may possibly find applications in metamaterial devices.

5 Reflectivity near the Dirac point

Near the Dirac point frequency ω_0, a lossless hypercrystal does not support propagating waves anywhere except in the direct proximity of the Brewser's momentum k_B. A study of the electromagnetic reflection from such composites would reveal a nearly 100% reflectivity anywhere aside from a narrow range near the Brewser's angle – see Fig. 9(a). Furthermore, when plotted in the angle-frequency coordinates, the reflection coefficient would clearly reveal the Dirac dispersion cone - as seen in Fig. 9(a).

The presence of material loss however substantially modifies this behavior. While the propagating modes in hypercrystals may have high Q-factors (see e.g. Figs. 4 and 6), the Dirac dispersion cones occupy a relatively narrow frequency

band $\delta\omega_D \ll \omega_0$. For the silicon-sapphire hypercrystal considered earliier, we find $\Delta\omega_D/\omega_0 \sim 10^{-2}$ (see Figs. 4(a) and 5). As a result, for this material system the imaginary part of the frequency is of the same order as the Dirac bandwidth, $\mathrm{Im}\,[\omega] \sim \Delta\omega_D$ – and the losses lead to a substantial modification of the reflectivity near the Dirac point.

However, while the sharp features of the Dirac dispersion cone in the reflectivity diagram of Fig. 9(a) are indeed washed out by the material loss, the resulting pattern still shows the signatures of the Dirac point – see Fig. 9(b). As a result, the non-monotonic behavior of the hypercrystal reflectivity observed in an experiment, can be used to locate the Dirac dispersion point.

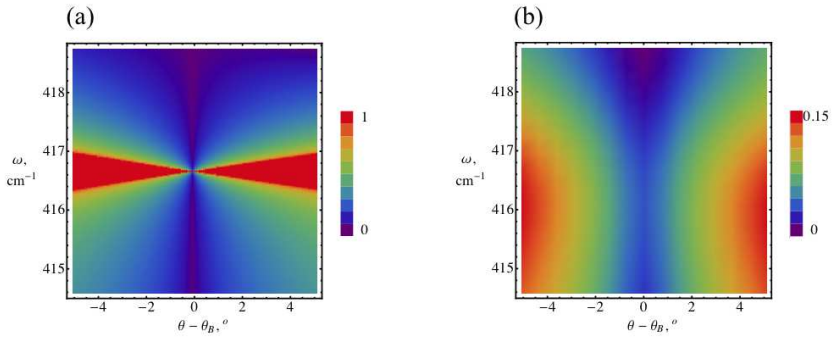

Fig. 9 The reflectivity of the interface of silicon and silicon-sapphire hypersrystal, in false-color representation. Panel (a) shows the lossless case, while the panel (b) includes the effects of material absorption. The angles θ and θ_B are respectively the incidence angle onto the hyper-crystal, and the Brewster's angle for the silicon-sapphire interface.

6 Motti singularity: Dirac points annihilation

While the study of the optical equivalents of both massless (Weyl-Dirac) and massive excitations offers many exciting opportunities,[3–9] in fundamental physics research as well as with an eye for possible applications, it may be beneficial to search for optical modes with a higher dispersion complexity. While the Lorenz invariance limits classical elementary particles to two mutually exclusive classes – bradyons[28] (with nonzero rest mass m_0), with the low kinetic energy limit

$$\mathcal{E} \simeq \frac{p^2}{2m_0} \tag{33}$$

and lyxons[29] ($m_0 = 0$), with the energy

$$\mathcal{E} = cp, \tag{34}$$

a meta-material quasi-particle can combine both kinds of classical motion:

$$\mathcal{E} = \sqrt{(cp_z)^2 + \left(\frac{p_x^2}{2m_0}\right)^2} \tag{35}$$

Probing such "mottion" excitations in an optical systems may offer interesting possibilities for e.g. novel electromagnetic resonant cavities that confine such modes, polarization control and phase matching in nonlinear-optical processes.

These "mottion" waves naturally arise in photonic hypercrystals at the Motti singularity[30] point of "annihilation" of two symmetry-related Dirac cones at $k_\tau = \pm k_B$. In a planar hypercrystal, this happens when the Dirac point frequency ω_0 approaches the frequency ω_M when the in-plane permittivity of the hyperbolic medium matches that of the isotropic component of the hypercrystal,

$$\varepsilon_\tau(\omega_M) \quad = \quad \varepsilon_i(\omega_M) \tag{36}$$

Within the bounds of the silicon-sapphire hypercrystal "platform", we can reach the critical point of (36) by controlled doping of the silicon layers. For n^+-doped silicon, the permittivity can be accurately described by the Drude model[31]

$$\varepsilon_{\rm Si} = \varepsilon_\infty \left(1 - \frac{\omega_p^2}{\omega(\omega + i\,\Gamma)}\right) \tag{37}$$

with $\varepsilon_\infty \approx 11.7$, $\omega_p = 10^{12}..10^{13}$ sec^{-1} (depending on the doping level) and $\Gamma \simeq 10^{11}..10^{12}$ sec^{-1}. For our example of the present section, we will choose $\omega_p = 250$ cm$^{-1} \equiv 7.5 \cdot 10^{12}$ sec^{-1}, which leads to the resonance (36) at the frequency ≈ 505 cm^{-1}, and neglect the loss in silicon compared to that in hyperbolic bands of sapphire. This behavior is illustrated in Fig. 10, where we plot the dielectric permittivities of both the doped silicon and sapphire, for the frequency range corresponding to second low-loss hyperbolic band of the latter.

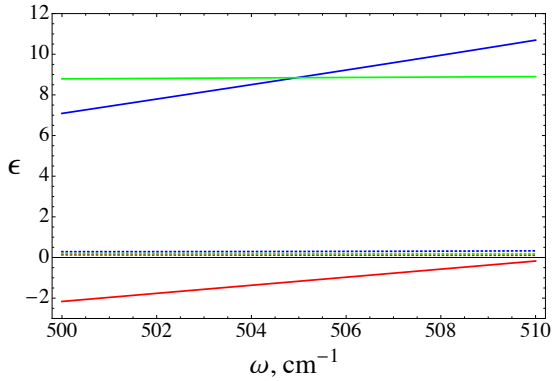

Fig. 10 The dielectric permittvities of doped silicon (green curves) and sapphire (red and blue curves for parallel (ε_n) and perpendicular (ε_τ) to the C-axis components respectively), for in the low-loss hyperbolic band near the free-space wavelength of 20 μm (≈ 500 cm^{-1}). Solid curves correspond to the real parts of the permittivities, while dotted lines represent the imaginary parts. Note that at $\omega \approx 505$ cm^{-1} we find $\varepsilon_\tau \approx \varepsilon_{\rm Si}$.

With the proper choice of the dimensions d_h and d_i of the unit cell of the hypercrystal, both Dirac points can be brought to "annihilation" at $(k_\tau, k_n) = (0,0)$, $\omega_0 = \omega_M$, resulting in the Motti singularity[30] of the photonic density of states of the hypercrystal. The resulting dispersion diagram can be described by

the effective Motti-Weyl Hamiltonian

$$\mathcal{H}_{\rm MW} = \begin{pmatrix} \frac{k_\tau^2}{2m_0} & -iv_n k_n \\ iv_n k_n & -\frac{k_\tau^2}{2m_0} \end{pmatrix} = \sigma_z \frac{k_\tau^2}{2m_0} + \sigma_y v_n k_n, \tag{38}$$

where σ_y and σ_z are the corresponding Pauli matrices. In Fig. 7 we present two orthogonal cross-sections of the exact dispersion diagram of the doped silicon-sapphire hypercrystal that supports the Motti singular point (36), clearly showing the mottion dispersion (35) of the effective Hamiltonian (38), $\mathcal{E}(k_\tau) \sim k_\tau^2$ and $\mathcal{E}(k_n) \sim |k_n|$.

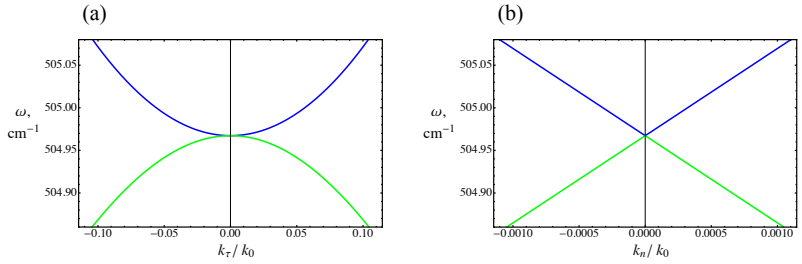

Fig. 11 The cross-sections of the doped silicon-sapphire hypercrystal dispersion that supports the Motti singularity at $\omega_0 = \omega_M \approx 504.97$ cm^{-1}, at $k_n = 0$ (panel (a)) and $k_\tau = 0$ (panel (b)), in the lossless limit. The unit cell of the hypercrystal is formed by $d_i \approx 6.11$ μm - thick layer of doped silicon and $d_h \approx 550$ nm-wide layer of sapphire. Note the "mottion" dispersion $\mathcal{E}(k_\tau) \sim k_\tau^2$, $\mathcal{E}(k_n) \sim |k_n|$ of the propagating waves in the hypercrystal near the Motti singularity point.

Similar to the Dirac point, the Motti singularity in the dispersion diagram of the hypercrystal also makes an imprint on the reflectivity of the composite. For a lossless system, at the singularity point we expect total reflectivity for any incidence angle $\theta \neq 0$. Furthermore, as a function of the frequency, the reflection coefficient would reveal the quadratic variation of the mottion dispersion (36) in the tangential direction,

$$\omega - \omega_M \propto \pm k_\tau^2. \tag{39}$$

This behavior is clearly seen in Fig. 11(a) that shows the reflectivity of the doped silicon-sapphire hypercrystal that supports the Motti singularity at the frequency $\omega_M \approx 505$ cm^{-1}, in the lossless limit.

While the actual material loss generally reduces the "contrast" of the propagating waves dispersion diagram "imprinted" onto the reflectivity of the hypercrystal, the calculation taking full account of the absorption in sapphire, still reveals the the mottion dispersion (36),(39) – see Fig. 12(b). Note that the width of the peak in reflectivity near the Motti singularity of the actual (lossy) hypercrystal, measured at half-maximum (when it drops from $\approx 80\%$ to $\approx 40\%$), is only 0.5 cm^{-1}, corresponding to barely 0.1% of the center frequency. Such relatively sharp features in a stronly absorbing system ($\mathrm{Im}[\varepsilon]/\mathrm{Re}[\varepsilon] \sim 10$ %) give a further indication for the essentially singular nature of the light transmission and

reflection in hypercrystal supporting the mottion resonance, and open the route to actual applications of optical hypercsrytals in practical nanophotonics.

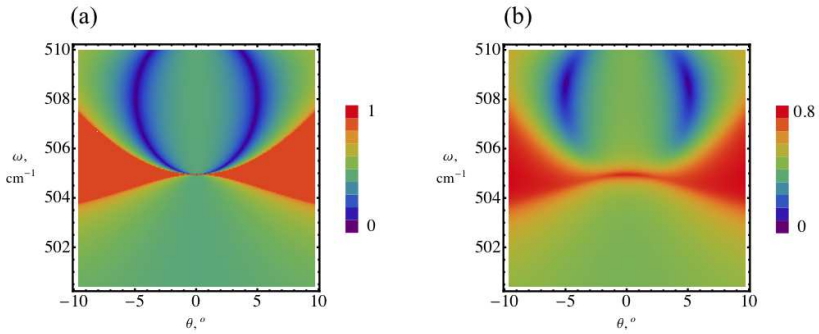

Fig. 12 The reflectivity of the interface of silicon and silicon-sapphire hypercrystal supporting Motti singularity near the frequency of 505 cm^{-1}, in the lossless approximation (a) and for the sapphire absorption taken into account (b). As in Fig. 9, here θ is the incidence angle onto the silicon-sapphire hypercrystal.

7 Conclusions

In conclusion, we have demonstrated that photonic hypercrystals allow Dirac-Weyl dispersion, as well as the Motti singularity at the annihilation of symmetry-related Dirac points. Despite relatively high loss in actual hypercrystals imposed by their hyperbolic consituents, the resulting sharp resonance structures in light propagation and reflection allow for both the study of optical analogues of such quantum phenomena as Shrödinger's zitterbewegung and Klein's tunneling, as well as for actual applications of these novel composite media in practical nanophotonics.

Acknowledgements

This work was partially supported by NSF Center for Photonics and Multiscale Metameterials, ARO MURI and Gordon and Betty Moore Foundation.

References

1 Y. Zhang, Y. W. Tan, H. L. Stormer, and P. Kim, "Experimental observation of the quantum Hall effect and Berrys phase in graphene," Nature **438**, 201 (2005).
2 A. H. C. Neto, F. Guinea, N. M. R. Peres, K. S. Novoselov, & A. K. Geim, "The electronic properties of graphene," Rev. Mod. Phys. **81**, 109 (2009).
3 L. G. Wang, Z. G. Wang, J. X. Zhang, & S. Y. Zhu, "Realization of Dirac point with double cones in optics," Opt. Lett. **34**, 1510 (2009).
4 R. A. Sepkhanov, Y. B. Bazaliy, & C. W. J. Beenakker, "Extremal transmission at the Dirac point of a photonic band structure," Phys. Rev. A **75**, 063813 (2007).
5 X. Zhang, "Observing zitterbewegung for photons near the Dirac point of a two-dimensional photonic crystal," Phys. Rev. Lett. **100**, 113903 (2008).

6 M. Diem, T. Koschny, & C. M. Soukoulis, "Transmission in the vicinity of the Dirac point in hexagonal photonic crystals," Physica B **405**, 2990 (2010).

7 F. Dreisow, M. Heinrich, R. Keil, A. Tnnermann, S. Nolte, S. Longhi, and A. Szameit, "Classical Simulation of Relativistic Zitterbewegung in Photonic Lattices," Phys. Rev. Lett. **105**, 143902 (2010).

8 X. Huang, Y. Lai, Z. H. Hang, H. Zheng and C. T. Chan, "Dirac cones induced by accidental degeneracy in photonic crystals and zero-refractive-index materials," Nature Materials **20**, 582 (2011).

9 O. Bahat-Treidel, O. Peleg, M. Grobman, N. Shapira, M. Segev, and T. Pereg-Barnea, "Klein Tunneling in Deformed Honeycomb Lattices," Phys. Rev. Lett. **104**, 063901 (2010).

10 O. Klein, "Die Reflexion von Elektronen an einem Potentialsprung nach der relativistischen Dynamik von Dirac," Zeitschrift für Physik **53** (34), 157 (1929).

11 E. Schrödinger, "Über die kräftefreie Bewegung in der relativistischen Quantenmechanik ("On the free movement in relativistic quantum mechanics"), Berliner Ber., 418 (1930); "Zur Quantendynamik des Elektrons," Berliner Ber, 63 (1931).

12 E. E. Narimanov, "Photonic Hypercrystals," Phys. Rev. X **4**, 041014 (2014).

13 Z. Jacob, L. V. Alekseyev, and E. E. Narimanov, "Optical Hyperlens: Far-field imaging beyond the diffraction limit," Optics Express **14**, 8247 (2006).

14 W. Cai and V. M. Shalaev, *Optical Metamaterials* (Springer, 2010).

15 J. D. Joannopoulos, S. G. Johnson, J. N. Winn, and R. D. Meade, *Photonic Crystals: Molding the Flow of Light* (Princeton University Press, 2008).

16 M. Schubert, T. E. Tiwald, and C. M. Herzinger, Infrared dielectric anisotropy and phonon modes of sapphire, Phys. Rev. B **61** (12), 8187 (2000).

17 J. Sun, J. Zhou, B. Li, and F. Kang, "Indefinite permittivity and negative refraction in natural material: graphite," Appl. Phys. Lett. **98** (10), 101901 (2011).

18 A. Hadni and X. Gerbaux, "Far IR excitation of longitudinal optical phonons in triglycine sulphate", Ferroelectrics **248**, 15 (2000).

19 X. Gerbaux, M. Tazawa, and A. Hadni, "Far IR transmission measurements on triglycine sulphate (TGS), at 5K," Ferroelectrics **215**, 47 (1998).

20 T. Dumelow, J. A. P. da Costa, and V. N. Freire, "Slab lenses from simple anisotropic media," Phys. Rev. B **72**, 235115 (2005).

21 W. S. Boyle, A. D. Brailsford, and J. K. Galt, "Dielectric anomalies and cyclotron absorption in the infrared: observations on bismuth," Phys. Rev. **109** (4), 1396 (1958).

22 W. S. Boyle and A. D. Brailsford, "Far infrared studies of bismuth," Phys. Rev. **120** (6), 1943 (1960).

23 V. D. Kulakovskii and V. D. Egorov, "Plasma reflection in bismuth and bismuth-antimony alloys," Sov. Phys. Solid State **15** (7), 1368 (1974).

24 L. V. Alekseyev, V. A. Podolskiy, and E. E. Narimanov, "Homogeneous hyperbolic systems for terahertz and far-infrared frequencies," Adv. OptoElectron. **2012**, 267564 (2012).

25 A. J. Hoffman, L. V. Alekseyev, S. S. Howard, K. J. Franz, D. Wasserman, V. A. Podolskiy, E. E. Narimanov, D. L. Sivco and C. Gmachl, "Negative refraction in semiconductor metamaterials," Nature Materials **6**, 948 (2007).

26 H. M. Manasevit, W. J. Simpson, "Single-Crystal Silicon on a Sapphire Substrate," Journal of Applied Physics **35**, 1349, (1964).

27 P. Yeh, *Optical Waves in Layered Media* (Wiley, 2005).

28 Which may also referred to as "tardyons" or "ittyons"[29].

29 O.-M. P. Bilaniuk, E. C. G. Sudarshan, "Particles beyond the Light Barrier," Physics Today **22** (5), 43 (1969).

30 P. M. Morse and H. Feshbah, *Methods of Theoretical Physics* (McGraw-Hill, 1953).

31 M. van Exter and D. Grischkowski, "Optical and electronic properties of doped silicon from 01. to 2 THz", Appl. Phys. Lett. **56** (17), 1694 (1990).